

RESEARCH ARTICLE | SEPTEMBER 01 2021

## Diffusion of gravity waves by random space inhomogeneities in pancake-ice fields. Theory and validation with wave buoys and synthetic aperture radar

Piero Olla   ; Giacomo De Carolis  ; Francesca De Santi 

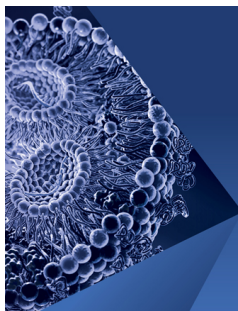


*Physics of Fluids* 33, 096601 (2021)

<https://doi.org/10.1063/5.0061374>



CrossMark



## Physics of Fluids

Special Topic:

Flow and Lipid Nanoparticles

Guest Editors: Richard Braatz and Mona Kanso

[Submit Today!](#)

# Diffusion of gravity waves by random space inhomogeneities in pancake-ice fields. Theory and validation with wave buoys and synthetic aperture radar

Cite as: Phys. Fluids **33**, 096601 (2021); doi: [10.1063/5.0061374](https://doi.org/10.1063/5.0061374)

Submitted: 25 June 2021 · Accepted: 11 August 2021 ·

Published Online: 1 September 2021



View Online



Export Citation



CrossMark

Piero Olla,<sup>1,a)</sup>  Giacomo De Carolis,<sup>2</sup>  and Francesca De Santi<sup>2</sup> 

## AFFILIATIONS

<sup>1</sup>ISAC-CNR, Sez. Cagliari, I-09042 Monserrato, Italy

<sup>2</sup>IREA-CNR, Sez. Milano, I-20133 Milano, Italy

<sup>a)</sup>Also at: INFN, Sez. Cagliari, I-09042 Monserrato, Italy. Author to whom correspondence should be addressed: [olla@dsf.unica.it](mailto:olla@dsf.unica.it)

## ABSTRACT

We study the diffusion of ocean waves by ice bodies much smaller than a wavelength, such as pancakes and small ice floes. We argue that inhomogeneities in the ice cover at scales comparable to that of the wavelength significantly increase diffusion, producing a contribution to wave attenuation comparable to what is observed in the field and usually explained by viscous effects. The resulting attenuation spectrum is characterized by a peak at the scale of the inhomogeneities in the ice cover, which could explain the rollover of the attenuation profile at small wavelengths observed in field experiments. The proposed attenuation mechanism leads to the same behaviors that would be produced by a viscous wave model with effective viscosity linearly dependent on the ice thickness. This may explain recent findings that viscous wave models require a thickness-dependent viscosity to fit experimental attenuation data. Experimental validation is carried out using wave buoy attenuation data and synthetic aperture radar image analysis.

© 2021 Author(s). All article content, except where otherwise noted, is licensed under a Creative Commons Attribution (CC BY) license (<http://creativecommons.org/licenses/by/4.0/>). <https://doi.org/10.1063/5.0061374>

## I. INTRODUCTION

Ocean surface waves play an important role in the dynamics of sea ice in polar regions. The effect is particularly visible in the marginal ice zone (MIZ), which is the highly dynamical transition region separating the ice pack from the open ocean.<sup>1</sup> In the summer season, erosion of the pack and breakup of large flows into smaller ice bodies are the dominant processes in the region. During winter, waves infiltrating the MIZ contribute to ice formation through the coalescence of ice bodies into progressively larger objects.<sup>2</sup> Global warming has led to an increase in both the activity and the extension of the MIZ. The Arctic in particular has seen a dramatic summertime increase in the MIZ extension and a concomitant reduction of the ice surface.<sup>3,4</sup> To determine how deep ocean waves can propagate into the MIZ, one must know the sea ice contribution to wave damping. Over the years, a great effort has been put into studying the modifications in surface wave propagation induced by sea ice (see Squire<sup>1,5,6</sup> for an extended review). In particular, remote sensing analysis of the modifications to wave

propagation by sea ice has been used as a tool to infer the ice thickness without having to resort to *in situ* measurements.<sup>7–14</sup>

Wave attenuation depends on the characteristic size of the ice bodies involved. In the case of larger floes on the scale of tens to hundreds of meters, scattering and diffraction,<sup>15,16</sup> as well as flexural deformations of the floes,<sup>17,18</sup> are expected to dominate (see Li *et al.*<sup>19</sup> for a recent application of thin plate theory to wave propagation in water covered by a continuous ice sheet). On the other hand, in the case of smaller ice bodies, viscous effects and collisions are expected to be dominant.<sup>20,21</sup> The picture is complicated by the strong inhomogeneity of the MIZ; although small ice is prevalent at the fringes of the MIZ, ice bodies of widely different sizes and typology can be found anywhere in the region.<sup>22</sup>

The focus of the present paper is the modification of ocean wave propagation produced by ice bodies much smaller than a wavelength, in particular pancake-ice. Pancake-ice is the assembly of pancake-shaped ice bodies of diameters ranging from 30 cm to 3 m, which populate,

during ice formation, the outer fringes of the MIZ.<sup>23,24</sup> It usually comes as a component of so-called grease-pancake ice (GPI), i.e., pancake-ice embedded in a dense slurry of ice crystals, called grease ice.

Grease ice is a strongly viscous medium, which is usually treated as a viscous continuum.<sup>25</sup> Over the years, various extensions of the viscous model have been proposed, such as the inclusion of viscoelasticity in the ice response<sup>26,27</sup> and of turbulent effects in the water under the ice<sup>28</sup> and the treatment of pancakes as an individual layer separate from grease ice.<sup>29</sup>

Providing a microscopic explanation for the effective viscosity of GPI, however, has proven problematic. This is reflected in the wide variation of the values of the parameters required to fit different experimental data sets.<sup>30,31</sup> The difficulty is compounded by recent observations<sup>14,24,32,33</sup> that most viscous layer models require an effective viscosity dependent on the ice thickness to fit available experimental data. The possibility that an intensive quantity such as the ice viscosity depends on a macroscopic quantity such as the ice layer thickness casts doubts on whether GPI could be treated as a simple viscous medium. Besides, there are situations in which pancakes (or other forms of multi-year small-scale or brash ice) float in low-viscosity grease-ice-free water.<sup>4</sup>

Another difficulty is that current viscous models are unable to explain the rollover effect, i.e., the decrease in wave attenuation at short wavelengths which is often observed in field measurements. Although this phenomenon has been discussed for over four decades, it still lacks an exhaustive explanation. The rollover effect has been so far ascribed to instrumental noise,<sup>34</sup> to exogenous mechanisms not properly taken into account, such as the energy input by the wind,<sup>33</sup> and to the effect of nonlinearities.<sup>35</sup> A possible explanation of the phenomenon was proposed by Liu and Mollo-Christensen,<sup>36</sup> as the result of the development of a viscous boundary layer under a continuous ice sheet treated as a thin elastic plate. Another explanation of the phenomenon was proposed by Perrie and Hu,<sup>37</sup> who performed numerical simulations with constant wind and regular arrays of medium size circular ice floes (diameter 20 m), suggesting that rollover is indeed the result of wave scattering. To our knowledge, however, scattering theory has never been applied at pancake scales yet.

All these remarks call for a reappraisal of alternative mechanisms of wave attenuation, such as, e.g., collisions between ice bodies,<sup>38</sup> nonlinear forces, and turbulence induced in the surrounding water by the ice motion.<sup>39</sup>

Purpose of the present study is to evaluate the scattering contribution to wave attenuation. We show that random inhomogeneities in the ice cover generate a coherent scattering component that can contribute significantly to wave damping. The phenomenon is akin to the enhancement of light scattering in a turbid medium. The approach we are going to follow is common to that for larger floes and is based on partial wave expansion of the flow disturbances generated by the inhomogeneities of the ice cover.<sup>40</sup> The nature of the scattering process in the case of floating bodies much smaller than a wavelength, however, is fundamentally different, as bodies within a wavelength respond coherently to the wave, and subtle near-field effects simplify the treatment of the scattering dynamics.

We assume potential flow for both the incident wave and the disturbances, thus disregarding viscous effects from the possible presence of grease ice at the water surface. Small amplitude waves and linear hydrodynamics are assumed throughout the analysis, and for simplicity, only the case of deep water waves is considered. We treat the ice layer as an

inextensible continuum with vanishing resistance to bending and with a rough bottom. In the case of a spatially uniform layer and no roughness, the dynamics reduces to that of the mass-loading model.<sup>41,42</sup>

We compare our theoretical results with experimental data from wave buoys collected during the Sikuliaq campaign in Autumn 2015.<sup>4</sup> By exploiting the availability of attendant satellite synthetic aperture radar (SAR) images available, it is possible to estimate the scale of the ice cover spatial inhomogeneities, which appears to coincide with that of the rollover peak.

The paper is organized as follows: In Sec. II, the general theory of scattering of gravity waves by floating bodies is reviewed. In Secs. III and IV, we apply the theory to determine the modification to the wavefield generated by random spatial variations in a continuous cover. In Sec. V, the consequences of the results on wave attenuation are discussed. In Sec. VI, the specific example of a spatially inhomogeneous mass loading with a rough ice-water interface is considered. In Sec. VII, current results are contextualized to the other wave propagation models in the literature. Section VIII contains a comparison with experimental data. Concluding remarks are reported in Sec. IX.

## II. PARTIAL WAVE EXPANSION

The study of the scattering of ocean waves by solid obstacles has a long history, which makes extensive use of techniques drawn from the study of similar problems in electromagnetism, acoustics, and quantum mechanics. The approach has been detailed elsewhere (see, e.g., Peter and Meylan<sup>43</sup>). We outline here the essentials.

The wave dynamics obeys the linearized Euler equation

$$\rho \partial_t \mathbf{U} + \nabla P = 0, \quad \nabla \cdot \mathbf{U} = 0, \quad (1)$$

where  $\mathbf{U}(\mathbf{x}, t)$  is the fluid velocity,  $\rho \simeq 1025 \text{ kg m}^{-3}$  is the salt water density,  $P(\mathbf{x}, t)$  is the deviation of the pressure in the water column from its value at hydrostatic equilibrium, and we have put the unperturbed water surface at  $x_3 = 0$  with  $\mathbf{e}_3$  pointing upwards. Equation (1) implies potential flow

$$\mathbf{U} = -\nabla \Phi, \quad \nabla^2 \Phi = 0. \quad (2)$$

Continuity of the pressure at the water surface,  $P(\mathbf{x}(t), t)|_{x_3=0} = 0$ , where  $\mathbf{x}(t)$  is the instantaneous position of the point at the water-atmosphere interface, leads to the boundary condition<sup>44</sup> on Eq. (2),

$$\left( \frac{\partial^2 \Phi}{\partial t^2} + g \frac{\partial \Phi}{\partial x_3} \right)_{x_3=0} = 0. \quad (3)$$

The wave energy contains both potential and kinetic energy contributions. We can eliminate the potential energy component by averaging over a suitable time window  $w$  and thus get the expression for the time averaged wave energy density

$$\mathcal{E}_\Phi(\mathbf{x}_\perp, t) = \frac{\rho}{2} \int_{-\infty}^0 dx_3 \langle |\mathbf{U}(\mathbf{x}, t)|^2 \rangle_w, \quad (4)$$

where  $\mathbf{x} = (\mathbf{x}_\perp, x_3)$  and  $\langle \cdot \rangle_w$  indicates time average in  $w$ . By comparing Eq. (4) with Eqs. (2) and (3), we find the conservation law

$$\partial_t \mathcal{E}_\Phi + \nabla_\perp \cdot \mathbf{J}_\Phi = 0, \quad \mathbf{J}_\Phi(\mathbf{x}_\perp, t) = \int_{-\infty}^0 dx_3 \langle P(\mathbf{x}, t) \mathbf{U}_\perp(\mathbf{x}, t) \rangle_w. \quad (5)$$

We assume elastic scattering, which implies linearity of possible mechanical interactions of the floating bodies; linear hydrodynamics then implies that the scattered waves oscillate with the same frequency

TABLE I. Relevant scales of the problem.

Near field $kL \ll 1$	Pancake scale $L \sim R$	Pancake geometry important
Wave region $kL \sim 1$	Intermediate scale $L \gg R$	Multipole expansion approach
Far field $kL \gg 1$	Diffused waves	

of the incident wave. In the case of a monochromatic incident wave of frequency  $\omega$ , the energy current  $\mathbf{J}_\Phi$  will satisfy

$$\mathbf{J}_\Phi = i\rho\omega \int_{-\infty}^0 dx_3 [\Phi \nabla_\perp \Phi^* - \Phi^* \nabla_\perp \Phi]. \quad (6)$$

We are interested in the scattering by ice bodies of characteristic size  $R$  much less than a wavelength. Taking inspiration from the treatment of similar problems in the case of electromagnetic radiation,<sup>45</sup> we separate in the potential a near-field component  $\phi$  from disturbances from bodies at distance  $\ll k^{-1}$  from  $\mathbf{x}$ , and a remnant  $\Psi$  containing the incident and the diffused waves:

$$\Phi(\mathbf{x}, t) = \Psi(\mathbf{x}, t) + \phi(\mathbf{x}, t). \quad (7)$$

A summary of the relevant scales in the problem is provided in Table I.

We are interested in the scattering by random space inhomogeneity of the ice cover. Let us then indicate with overbar the operation of ensemble average with respect to the inhomogeneities of the ice cover, with tilde fluctuation and decompose the generic physical quantity  $f$  accordingly:

$$f = \bar{f} + \tilde{f}. \quad (8)$$

Hence,  $\bar{\Psi}$  contains the incident wave,  $\tilde{\Psi}$  contains the diffused waves; ensemble averaging and coarse-graining have the same filtering effect on the small scales, therefore  $\bar{\Phi} = \bar{\Psi}$  and  $\phi = \tilde{\phi}$ . Consider a portion  $A$  of unperturbed water surface at  $\mathbf{x}_\perp = 0$  and indicate with  $\tilde{\Psi}_A$  the contribution to wave diffusion from the bodies in that region. The geometry of the problem is sketched in Fig. 1. Let us assume a monochromatic incident wave propagating to positive  $x_1$ :  $\mathbf{k} = k\mathbf{e}_1$ ; from Eqs. (2) and (3), we then get the classical deep-water surface gravity wave solution in ice-free water

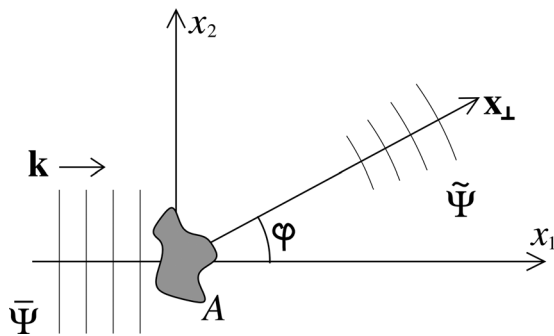


FIG. 1. Geometry of the problem.

$$\bar{\Psi}(\mathbf{x}, t) = \bar{\Psi}_0(t) \exp(kx_3 + ikx_1) = \bar{\Psi}_0 \exp[kx_3 + i(kx_1 - \omega t)], \quad \omega^2 = kg. \quad (9)$$

We can expand the incident wave in partial waves

$$\bar{\Psi}(\mathbf{x}, t) = \bar{\Psi}(t) \left[ J_0(kx_\perp) + 2 \sum_{n=1}^{\infty} i^n J_n(kx_\perp) \cos(n\varphi) \right] e^{kx_3}, \quad (10)$$

and similarly for  $\Psi_A = \bar{\Psi} + \tilde{\Psi}_A$ ,

$$\Psi_A(\mathbf{x}, t) = \tilde{\Psi}_{A,eva}(\mathbf{x}, t) + \bar{\Psi}_0(t) \left[ B_0 J_0(kx_\perp) + C_0 N_0(kx_\perp) + 2 \sum_{n=1}^{\infty} i^n (B_n J_n(kx_\perp) + iC_n N_n(kx_\perp)) \cos(n\varphi) \right] e^{kx_3}, \quad (11)$$

where  $\cos \varphi = x_1/x_\perp$ ,  $J_n$  and  $N_n$  are Bessel functions of the first and second kind, respectively, and  $\tilde{\Psi}_{A,eva}$  contains evanescent modes, which can be expressed in terms of modified Bessel functions  $K_n$ , exponentially decaying at large  $kx_\perp$ .<sup>46</sup> The evanescent modes can be disregarded in the far-field region, and the remaining part of  $\Psi_A$  is a sum of outward and inward propagating modes  $\propto e^{\pm ikx_\perp}$ . Requiring  $\tilde{\Psi}_A$  not to contain inward propagating modes (Sommerfeld condition), together with stationarity,  $\mathbf{J}_{\tilde{\Psi}} = 0$ , allows us to fix the coefficients in Eq. (11).<sup>47</sup> This gives us the expression for the perturbed field in the far-field region  $kx_\perp \gg 1$

$$\tilde{\Psi}_A(\mathbf{x}, t) = \bar{\Psi}_0(t) \left[ \frac{e^{2i\delta_{A,0}-1}}{2} H_0^{(1)}(kx_\perp) + \sum_{n=1}^{\infty} i^n (e^{2i\delta_{A,n}} - 1) \times H_n^{(1)}(kx_\perp) \cos(n\varphi) \right] e^{kx_3}, \quad kx_\perp \gg 1, \quad (12)$$

where  $H_n^{(1)} = J_n + iN_n$  are Hankel function of the first kind,<sup>46</sup> and the coefficients  $\delta_{A,n}$  are real constants called the scattering phases.

We confine our attention to situations in which scattering can be considered a perturbation; the scattering phases therefore are small, and we can linearize Eq. (12):

$$\tilde{\Psi}_A(\mathbf{x}, t) \equiv \sum_n \tilde{\Psi}_{A,n}(\mathbf{x}, t) \simeq i\bar{\Psi}_0(t) \left[ \delta_{A,0} H_0^{(1)}(kx_\perp) + 2 \sum_{n=1}^{\infty} i^n \delta_{A,n} H_n^{(1)}(kx_\perp) \cos(n\varphi) \right] e^{kx_3}, \quad kx_\perp \gg 1. \quad (13)$$

Let us suppose that  $A$  contains all the bodies responsible for scattering, or equivalently that the interference with waves scattered by bodies outside  $A$  is negligible. In this case, the radiated energy is

$$I_{\tilde{\Psi}_A} = \int_0^{2\pi} d\varphi \mathbf{x}_\perp \cdot \mathbf{J}_{\tilde{\Psi}_A}(\mathbf{x}), \quad (14)$$

where  $\mathbf{J}_{\tilde{\Psi}_A}$  is obtained from Eq. (6) by replacing  $\Phi$  with  $\tilde{\Psi}_A$ . Substituting Eq. (13) into Eq. (14) and exploiting the relation<sup>46</sup>  $N'_n(z)J_n(z) - N_n(z)J'_n(z) = 2/(\pi z)$  yields

$$I_{\bar{\Psi}_A} \equiv \sum_n I_{\bar{\Psi}_{A,n}} = \int_0^{2\pi} d\varphi \mathbf{x}_\perp \cdot \mathbf{J}_{\bar{\Psi}_A}(\mathbf{x}) \simeq \frac{4\rho\omega|\bar{\Psi}_0|^2}{k} \sum_{n=0}^{\infty} \delta_{A,n}^2. \quad (15)$$

By combining Eq. (15) with the energy flux density of the incident wave

$$\mathbf{J}_{\bar{\Psi}} = \omega\rho|\bar{\Psi}_0|^2 \mathbf{e}_1, \quad (16)$$

we obtain the expression for the scattering cross section

$$\sigma_A = \frac{I_{\bar{\Psi}_A}}{J_{\bar{\Psi}}} \simeq 4k^{-1} \sum_{n=0}^{\infty} \delta_{A,n}^2. \quad (17)$$

### III. THE NEAR FIELD

Let us consider a region  $A$  at the water surface around  $x_\perp = 0$ , of size  $L_A$  sufficiently large to carry out a continuous limit, but small compared to the wavelength:  $R \ll L_A \ll k^{-1}$ . The near-field disturbance by the bodies in  $A$  is a complicated superposition of propagating and evanescent modes,<sup>40,48</sup> which is more aptly analyzed by making the decomposition  $\phi_A = \phi_{A,reg} + \phi_{A,sing}$ , where  $\phi_{A,reg}$  and  $\phi_{A,sing}$  are the regular (singular) components of  $\phi$  at  $\mathbf{x}_\perp = 0$ ,  $R, L \rightarrow 0$ , and both components are required to decay for  $x_\perp \rightarrow \infty$ .

The regular component can only contain Bessel functions  $J_n$ . We therefore obtain from Eq. (13) the expression, valid for all  $kx_\perp$ ,

$$\begin{aligned} \phi_{A,reg} &\equiv \sum_n \phi_{A,reg,n} \\ &\simeq i\bar{\Psi}_0 \left[ \delta_0 J_0(kx_\perp) + 2 \sum_{n=1}^{\infty} i^n \delta_n J_n(kx_\perp) \cos(n\varphi) \right] e^{kx_3}. \end{aligned} \quad (18)$$

The singular component  $\phi_{A,sing}$  is a superposition of Bessel functions  $N_n$  and  $K_n$ , out of which, only the  $N_n$  component survives in the far-field region  $kx_\perp \gg 1$ , where it forms the imaginary part of the Hankel functions in Eq. (13). Let us focus on an intermediate region  $L_A \ll x_\perp \ll k^{-1}$  in the near field. We assume that the hydrodynamic interaction of the bodies decays sufficiently fast with their separation. In a first approximation, the perturbed potential  $\phi_{A,sing}$  can therefore be evaluated at  $x_\perp \gg L_A$  using the ice-free boundary condition in Eq. (3). In that region,  $\phi_{A,sing}$  sees  $A$  as a point and is expected to vary at scale  $x$ ; since the timescale of wave disturbances at scales  $x_\perp \ll k^{-1}$  is much shorter than  $\omega^{-1}$ , we can replace the Robin boundary condition in Eq. (3) with the Neumann boundary condition

$$\partial_{x_3} \phi_{A,sing}(\mathbf{x}, t)|_{x_3=0} = 0, \quad x_\perp \neq 0. \quad (19)$$

The perturbed potential  $\phi_{A,sing}$  will thus behave in the intermediate region like the electrostatic potential of a superposition of multipoles at  $\mathbf{x} = 0$ . This allows us to do away with the evaluation of evanescent and propagating modes in terms of Bessel functions. Linearity of the dynamics allows us to write the perturbed potential in the form

$$\begin{aligned} \phi_{A,sing}(\mathbf{x}, t) &\equiv \sum_n \phi_{A,sing,n}(\mathbf{x}, t) \\ &\simeq \frac{1}{2\pi} \left[ \frac{\alpha_{A,0}}{x} + \frac{\alpha_{A,1} \cdot \mathbf{x}_\perp}{x^3} + \frac{\alpha_{A,2} : \mathbf{x}_\perp \mathbf{x}_\perp}{x^5} + \dots \right] \bar{\Psi}_0(\mathbf{x}, t), \end{aligned} \quad (20)$$

where the  $\alpha_{A,n}$ 's are  $n$ -index symmetric zero-trace tensors playing a role analogous to the polarizability of a small body in the field of an electromagnetic wave, which enter Eq. (20) contracted with  $n$  terms  $\mathbf{x}'_\perp$  and with a weigh factor  $x^{-1-2n}$ .

We can write Eq. (20) as a surface integral at  $x'_3 = 0$ :

$$\begin{aligned} \phi_{A,sing}(\mathbf{x}, t) &= \frac{1}{2\pi} \int_A d^2x'_\perp \bar{\Psi}(\mathbf{x}', t) \delta(\mathbf{x}'_\perp) \\ &\quad \times [\alpha_{A,0}(\mathbf{x}'_\perp) + \alpha_{A,1}(\mathbf{x}'_\perp) \cdot \nabla'_\perp + \dots] |\mathbf{x} - \mathbf{x}'|^{-1} \\ &= \frac{1}{2\pi} \int_A d^2x'_\perp |\mathbf{x} - \mathbf{x}'|^{-1} \\ &\quad \times [\alpha_{A,0}(\mathbf{x}'_\perp) - \nabla'_\perp \cdot \alpha_{A,1}(\mathbf{x}'_\perp) + \dots] \bar{\Psi}(\mathbf{x}', t) \delta(\mathbf{x}'_\perp), \end{aligned}$$

where in the second line of the equation the horizontal gradient  $\nabla'_\perp$  acts both on  $\alpha_{A,1}(\mathbf{x}'_\perp)$  and on the factors  $\bar{\Psi}(\mathbf{x}', t) \delta(\mathbf{x}'_\perp)$  to the right of the square brackets. The surface charge distribution  $[\alpha_{A,0}(\mathbf{x}'_\perp) - \nabla'_\perp \cdot \alpha_{A,1}(\mathbf{x}'_\perp) + \dots] \bar{\Psi}(\mathbf{x}', t) \delta(\mathbf{x}'_\perp)$  induces the boundary condition on the Laplace equation<sup>45</sup>  $\nabla'^2 \phi_{A,sing} = 0$ :

$$\partial_{x_3} \phi_{A,sing}(\mathbf{x}, t)|_{x_3=0} = [\alpha_{A,0}(\mathbf{x}_\perp) - \nabla_\perp \cdot \alpha_{A,1}(\mathbf{x}_\perp) + \dots] \bar{\Psi}(\mathbf{x}, t) \delta(\mathbf{x}_\perp). \quad (21)$$

Equation (21) tells us that the effect of the bodies in  $A$  is a localized perturbation of the vertical component of the fluid velocity at the surface. The situation is particularly clear in the case of an isolated body. If we take  $A$  to coincide with the horizontal section of the body at  $x_3 = 0$ ,  $V_3 = -\alpha_{A,0} \bar{\Psi}/A$  will be precisely the vertical velocity of the body relative to the water surface.

The next contribution is a dipole, which accounts for the horizontal motion of the body with respect to the wave. We have

$$\frac{\alpha_{A,1} \bar{\Psi}_0}{2\pi} = -\frac{1}{2\pi} \int_S dS \mathbf{x} \partial_n \phi_{A,sing}(\mathbf{x}) = \frac{1}{2\pi} \int_S dS \mathbf{x} V_n(\mathbf{x}), \quad (22)$$

where  $\mathbf{n}(\mathbf{x})$  is the normal at point  $\mathbf{x}$  on the submerged part  $S$  of the body surface and  $\mathbf{V}$  is the velocity of the body relative to the wave field. In the case of a fixed horizontal disk, such that  $\mathbf{V} = -\mathbf{U}$ , we would have

$$\alpha_{A,1} \simeq i\pi k R^2 h \mathbf{e}_1, \quad (23)$$

where  $h$  and  $R$  are the draft and the radius of the disk.

Higher order multipoles take into account the effect of the non-uniformity of the velocity field of the wave at the scale of the body and involve additional factors  $kR$ . For small  $kR$ , they can therefore be disregarded.

### IV. THE FAR FIELD

Let us now take for  $A$  a region of size  $L_A \gg \lambda$ , where  $\lambda$  is the correlation length of the fluctuations in the ice cover. Since we are assuming  $\lambda$  comparable with the wavelength of the incident waves, the area element  $A$  in Sec. III must be considered infinitesimal compared to the one we are dealing with here. We introduce intensive quantities

$$\chi_n = \frac{d\alpha_n}{dA}(\mathbf{x}_\perp) \quad (24)$$

giving the susceptibility of the medium. We assume local isotropy of the ice cover, so that  $\chi_1 = \chi_1 \mathbf{e}_1$ , with similar expressions holding for higher-order multipoles.

At scales  $x_{\perp} \geq k^{-1}$ , the time derivative in the boundary condition Eq. (21) must be restored:

$$(g\partial_{x_3} - \omega^2)\Psi|_{x_3=0} \simeq g\tilde{\chi}\bar{\Psi}|_{x_3=0} \equiv [\chi_0 - \nabla_{\perp} \cdot (\boldsymbol{\chi}_1\bar{\Psi})]_{x_3=0}. \quad (25)$$

Equations for the mean and the fluctuating components of  $\Psi$  can be obtained from Eq. (25) by following the strategy described in Howe.<sup>49</sup> We find

$$\nabla^2\bar{\Psi} = \nabla^2\tilde{\Psi} = 0, \quad (26)$$

$$(g\partial_{x_3} - \omega^2)\bar{\Psi}|_{x_3=0} = g[\tilde{\chi}\bar{\Psi} + \tilde{\chi}\bar{\Psi}]_{x_3=0}, \quad (27)$$

$$(g\partial_{x_3} - \omega^2)\tilde{\Psi}|_{x_3=0} = g[\tilde{\chi}\bar{\Psi} + \tilde{\chi}\tilde{\Psi} + \tilde{\chi}\tilde{\Psi} - \tilde{\chi}\tilde{\Psi}]_{x_3=0}. \quad (28)$$

For  $\chi \ll 1$ , Eqs. (27) and (28) approximate to

$$(g\partial_{x_3} - \omega^2)\bar{\Psi}(\mathbf{x}, t)|_{x_3=0} \simeq g\tilde{\chi}\bar{\Psi}(\mathbf{x}, t)|_{x_3=0}, \quad (29)$$

$$(g\partial_{x_3} - \omega^2)\tilde{\Psi}(\mathbf{x}, t)|_{x_3=0} \simeq g\tilde{\chi}\tilde{\Psi}(\mathbf{x}, t)|_{x_3=0}. \quad (30)$$

From Eq. (29), we get the dispersion relation in the ice covered region

$$kg \simeq (1 + \bar{\chi}/k)\omega^2, \quad (31)$$

where  $1 + \bar{\chi}/k \simeq 1 + \bar{\chi}_0/k - i\bar{\chi}_1$  plays the role of (average) refractive index of the medium. For  $\bar{\chi} = 0$ , the dispersion relation for gravity waves in ice-free deep water,  $kg = \omega^2$ , is recovered.

### A. Fluctuating component

The fluctuating component of the far-field  $\tilde{\Psi}$  contains the diffused waves. We can solve Eq. (30) by requiring in the near and far field, equality of the values of the energy flux which would be generated by each element  $dA$  of the ice field in isolation.

Let us indicate with  $\delta_{dA,n}$  and with  $\tilde{\alpha}_{dA,n} = \tilde{\chi}_n dA$  the scattering phase and the polarizability fluctuation of the area element. The value of the energy flux in the near-field region is obtained by combining Eqs. (6), (18), and (20)

$$\begin{aligned} I_{\phi_{dA,n}} &= i(2 - \delta_{n0})x_{\perp}\rho\omega \int_0^{2\pi} d\varphi \\ &\times \left\{ \phi_{dA,reg,n} \int_{-\infty}^0 \partial_{\perp} \phi_{dA,sing,n}^* dx_3 - c.c. \right\}_{x_{\perp}=0} \\ &\simeq (2n+1)i^n \rho\omega \delta_{dA,n} \tilde{\alpha}_{dA,n}^* |\bar{\Psi}_0|^2 \\ &\times \left[ x_{\perp}^{2+n} J_n(kx_{\perp}) \int_{-\infty}^0 \frac{dx_3}{(x_{\perp}^2 + x_3^2)^{n+3/2}} \right]_{x_{\perp}=0} \\ &= \frac{(2n+1)\sqrt{\pi}}{2^{n+1}\Gamma(n+3/2)} \rho\omega (ik)^n \delta_{dA,n} \tilde{\alpha}_{dA,n}^* |\bar{\Psi}_0|^2, \end{aligned} \quad (32)$$

where the  $\delta_{n0}$  in the first line of the equation is a Kronecker delta, and use has been made of the expression for small values of the argument of the Bessel function  $J_n(z) \simeq (z/2)^n / \Gamma(n+1)$ .<sup>46</sup> The same flux evaluated in the far-field region reads, from Eq. (15),

$$I_{\tilde{\Psi}_{dA,n}} = \frac{4\rho\omega |\bar{\Psi}_0|^2}{k} \delta_{dA,n}^2. \quad (33)$$

Requiring equality of the expressions in Eqs. (32) and (33) yields then

$$\delta_{dA,n} \simeq \frac{(2n+1)\sqrt{\pi}i^n k^{n+1} \tilde{\chi}_n^*}{2^{n+3}\Gamma(n+3/2)} dA, \quad (34)$$

where from reality of  $\delta_{n0}$ ,  $\tilde{\chi}_{2n}$  must be real and  $\tilde{\chi}_{2n+1}$  purely imaginary.

For  $L_a \gg \lambda$ , the interference of waves generated in different regions  $A$  vanishes after ensemble averaging; the total diffused energy is therefore the sum of the energy diffused by the individual regions. At large distance from  $A$ , we can write from Eq. (13)

$$\begin{aligned} \tilde{\Psi}_{A,n}(\mathbf{x}, t) &\simeq i^{n+1}(2 - \delta_{0n})\bar{\Psi}_0(t)e^{kx_3} \cos(n\varphi) \\ &\times \int_A d^2x'_{\perp} \frac{d\delta_n}{dA}(\mathbf{x}'_{\perp}) H_n^{(1)}(k|\mathbf{x}_{\perp} - \mathbf{x}'_{\perp}|) \\ &\simeq i^{n+1}(2 - \delta_{0n})\bar{\Psi}_0(t)e^{kx_3} \cos(n\varphi) H_n^{(1)}(kx_{\perp}) \\ &\times \int_A d^2x'_{\perp} \frac{d\delta_n}{dA}(\mathbf{x}'_{\perp}) e^{i\mathbf{k}\cdot\mathbf{x}'_{\perp}}, \end{aligned} \quad (35)$$

where

$$\hat{\mathbf{k}} = \mathbf{k} - \frac{k\mathbf{x}_{\perp}}{x_{\perp}}, \quad (36)$$

and where the following asymptotic expression of the Hankel function for large values of the argument has been used:

$$H_n^{(1)}(y) \simeq \sqrt{\frac{2}{\pi|y|}} \exp\left[i\left(y - \frac{(2n+1)\pi}{4}\right)\right]. \quad (37)$$

From Eq. (34), we have  $d\delta_0/dA = k\tilde{\chi}_0/4$  and  $d\delta_1/dA = ik^2\tilde{\chi}_1^*/4$ , which we substitute into Eq. (35) and then into Eq. (6). We thus get the expressions for the energy density flux

$$\mathbf{x}_{\perp} \cdot \bar{\mathbf{J}}_A \simeq \frac{\rho kA\omega}{8\pi} |\bar{\Psi}_0|^2 X(\mathbf{k}, \varphi), \quad (38)$$

$$X(\mathbf{k}, \varphi) = X_0(\mathbf{k}, \varphi) + [1 + \cos(2\varphi)]k^2 X_1(\mathbf{k}, \varphi), \quad (39)$$

where

$$X_n(\mathbf{k}, \varphi) = (-1)^n \int d^2x_{\perp} \tilde{\chi}_n(\mathbf{x}_{\perp}) \tilde{\chi}_n(0) e^{i\mathbf{k}\cdot\mathbf{x}_{\perp}} \quad (40)$$

is the spectrum of  $\tilde{\chi}_n$  evaluated at  $\hat{\mathbf{k}} = \hat{\mathbf{k}}(\mathbf{k}, \varphi)$ , and where we have exploited the condition  $L_A \gg \lambda$  to set  $A \rightarrow \infty$  in Eq. (40).

We finally substitute Eq. (38) into Eq. (15) and into Eq. (17) and get the scattering cross-section of the ice in  $A$ :

$$\sigma_A(\mathbf{k}) \simeq \frac{kA}{8\pi} \int_{-\pi}^{\pi} d\varphi X(\mathbf{k}, \varphi). \quad (41)$$

### V. CONSEQUENCES ON WAVE ATTENUATION

The energy transfer to the diffused waves produces spatial attenuation of the incident wave with the rate

$$q(\mathbf{k}) = \frac{\sigma_A(\mathbf{k})}{A} \simeq \frac{k}{8\pi} \int_{-\pi}^{\pi} d\varphi X(\mathbf{k}, \varphi). \quad (42)$$

Since we are describing wave diffusion as the result of fluctuations in the refractive index of the ice cover, an important parameter is the

correlation length  $\lambda$  of the field  $\tilde{\chi}$ . We consider separately the two limits  $k\lambda \ll 1$  and  $k\lambda \gg 1$ .

### A. Small wavenumbers

For small  $k\lambda$ , we can carry out the  $k \rightarrow 0$  limit in Eq. (40); Eq. (42) reduces then to

$$q(\mathbf{k}) \simeq \frac{k\overline{\chi(\varphi)}}{4}, \quad k\lambda \ll 1, \quad (43)$$

and if  $X_1 = 0$ , scattering is isotropic.

We can apply the results to a random distribution of pointlike scattering centers of strength  $\delta_0 = k\alpha_0/4$ ,  $\delta_1 = 0$ , and surface density  $\bar{n}$ . We have the Poisson statistics result

$$\overline{\chi(\mathbf{x}_\perp)\chi(0)} = \frac{16\bar{n}\delta_0^2}{k^2} \delta(\mathbf{x}_\perp), \quad (44)$$

which, by substituting into Eqs. (41) and (42), gives us

$$q(\mathbf{k}) = \frac{4\bar{n}\delta_0^2}{k} = \bar{n}\sigma(\mathbf{k}), \quad \bar{n}R^2 \ll 1, \quad k\lambda \ll 1, \quad (45)$$

where  $\sigma = 4\delta_0^2/k$  is the cross-section of the individual scattering center. The result coincides with what would be obtained in the case of incoherent diffusion by scattering objects at separation larger than a wavelength. The situation is similar to that of the scattering of the light of the sun by air molecules, responsible for blue sky, an effect which can identically be described as the result of Rayleigh scattering by individual air molecules and that of refractive index fluctuations peaked at molecular scales.

### B. Large wavenumbers and possibility of rollover effects

For large  $k\lambda$ , scattering becomes progressively concentrated along  $\mathbf{k}$ . To illustrate the situation, we consider the case of Gaussian isotropic fluctuations,  $\overline{\chi(\mathbf{x}_\perp)\chi(0)} = \overline{\tilde{\chi}^2(\varphi)} \exp[-x_\perp^2/(2\lambda^2)]$ ,  $\overline{\tilde{\chi}^2(\varphi)} \equiv \overline{\tilde{\chi}_0^2} - k^2[1 + \cos(2\varphi)]\overline{\tilde{\chi}_1^2}$ , corresponding to the fluctuation spectrum,

$$X(\mathbf{k}, \varphi) = 2\pi\lambda^2\overline{\tilde{\chi}^2(\varphi)} \exp[-(k\lambda)^2(1 - \cos\varphi)]. \quad (46)$$

We can verify by direct substitution of Eq. (46) into Eq. (42), that, for large  $k\lambda$ , diffusion takes place at angles

$$|\varphi| \sim (k\lambda)^{-1}. \quad (47)$$

In realistic situations, however, the incident waves are not monochromatic; what one has instead is a distribution of waves peaked at  $\mathbf{e}_1$ , with a finite opening angle  $\varphi_{inc}$ . The role of directional spreading of waves in sea ice was recognized recently by Montiel *et al.*<sup>50</sup> To obtain the attenuation of the wave train, it is then necessary to consider the scattering of waves at angles  $|\varphi| > \varphi_{inc}$ , since smaller angles would be associated with a redistribution of the wave energy among modes within the wave train. We thus replace the definition of attenuation in Eq. (42) with

$$q_{eff}(\mathbf{k}) \simeq \frac{k}{8\pi} \int_{|\varphi| > \varphi_{inc}} d\varphi X(\mathbf{k}, \varphi). \quad (48)$$

We can substitute Eq. (46) into Eq. (48) and evaluate the resulting integral for large  $k$  by steepest descent. We obtain

$$q_{eff}(\mathbf{k}) \simeq \frac{\overline{\tilde{\chi}^2}(0)}{4k\varphi_{inc}} \exp\left(-\frac{(k\lambda\varphi_{inc})^2}{2}\right), \quad (k\lambda)^{-1} \ll \varphi_{inc} \ll 1, \quad (49)$$

which signals that a rollover effect is indeed present at wavenumbers

$$k_{roll}(\mathbf{k}) \sim (\lambda\varphi_{inc})^{-1}. \quad (50)$$

We note that the effect depends on our definition of  $q_{eff}$  as a loss of energy of waves at angles  $|\varphi| < \varphi_{inc}$ , without distinction of scattered and incident components. Infinite resolution and the ability to separate the incident and the diffused components in the wave field at angles  $|\varphi| < \varphi_{inc}$  would allow us to eliminate rollover. Substitution of Eq. (46) into Eq. (42) and evaluation of the resulting saddle point integral for  $k\lambda \gg 1$  would yield in this case

$$q_{eff}(\mathbf{k}) \sim \lambda\overline{\tilde{\chi}^2}(0), \quad \varphi_{inc} \ll (k\lambda)^{-1} \ll 1, \quad (51)$$

with just a slow down of attenuation increase at large  $k$ , compared to Eq. (43).

We point out that in realistic situations the energy spectrum of the incident waves does not have a sharp cutoff in direction, and the definition of the parameter  $\varphi_{inc}$  remains arbitrary; the only condition that must be satisfied is  $\varphi_{inc} < \pi/2$ . This freedom in the definition of  $\varphi_{inc}$  provides us with a possible test of the role of scattering in wave attenuation, since, if wave scattering is the mechanism underlying rollover, attenuation of waves in the angular interval  $|\varphi| < \varphi_{inc}$  should decrease in response to an increase in  $\varphi_{inc}$ . In the opposite limit  $k\lambda \ll 1$ , diffusion is isotropic and  $q_{eff} \approx q$  irrespective of the choice of  $\varphi_{inc}$ .

### VI. EVALUATION OF THE SUSCEPTIBILITY FUNCTION

Determining the susceptibility functions  $\chi_n$  requires knowledge of the coupled wave-ice dynamics at the scale of the individual ice bodies. A semi-quantitative description of the dynamics can be obtained by modeling the ice layer as a continuum that resists compression both horizontally and vertically but has a relatively low resistance to bending. This is the hypothesis at the basis of the mass-loading model,<sup>41,42,51</sup> which implies that points at the bottom and the top of the ice layer move with identical vertical velocity. We set indeed the resistance to bending equal to zero, thus disregarding any contribution to the dynamics from the bending rigidity of the ice bodies and the viscous stresses in the layer. Such contributions should probably be taken into account if the size of the ice bodies was comparable with the wavelength.

In the present hypotheses, the vertical velocity at the bottom of the ice layer differs by an amount

$$V_3(\mathbf{x}_\perp, t) = -h(\mathbf{x}_\perp)\partial_{x_3} U_3(\mathbf{x}, t)|_{x_3=0} = -k^2 h(\mathbf{x}_\perp)\bar{\Psi}(\mathbf{x}, t)|_{x_3=0}, \quad (52)$$

from its value  $\bar{U}_3(\mathbf{x}, t) = \bar{U}_3(\mathbf{x}, t)|_{x_3=0} + k^2\bar{\Psi}(\mathbf{x}, t)|_{x_3=0}h(x_\perp)$  in the absence of ice, where  $h(\mathbf{x}_\perp)$  is a vertical scale giving the local draft of the ice layer. From comparison with Eqs. (21) and (25), we get immediately

$$\chi_0(\mathbf{x}_\perp) = k^2 h(\mathbf{x}_\perp), \quad (53)$$

which is the same susceptibility that would be produced by a distribution of non-interacting ice bodies of horizontal size  $R$ , surface number density  $n \sim R^{-2}$ , and polarizability  $\alpha_0 \sim k^2 R^2 h$ . On the other hand,

because of horizontal incompressibility, the horizontal velocity of points in the ice layer is zero, and therefore

$$V_1 = -U_1|_{x_3=0}. \tag{54}$$

The bottom of the ice layer is an irregular surface with characteristic horizontal and vertical roughness scales fixed by  $R$  and  $h$ . Comparison of Eqs. (54) and (24) tells us then that the susceptibility function has a dipole component

$$\chi_1 \sim iCkhR^2n, \quad C = \pi R^2n. \tag{55}$$

Since for close-packed ice  $C \sim 1$ , the two contribution to susceptibility in Eqs. (53) and (55) enter Eq. (25) at the same order in  $kh$ . We then substitute Eqs. (53) and (55) into Eq. (31) and get the following renormalized version of the mass-loading model:

$$kg = [1 + (1 + r_1)k\bar{h}] \omega^2, \tag{56}$$

where  $r_1$  is a dimensionless constant which contains information on the local geometric structure of the ice layer and gives the strength of the roughness contribution to dispersion.

More interestingly, we can study the effect of spatial fluctuations in the layer structure on wave diffusion. For simplicity, we continue to assume a Gaussian profile for the correlations of  $\tilde{\chi}$ . Substituting Eqs. (53) and (55) into Eq. (46) yields then

$$X(\mathbf{k}, \varphi) = 2\pi k^4 \lambda^2 \bar{h}^2 \{1 + [1 + \cos(2\varphi)]r_2\} \times \exp[-(k\lambda)^2(1 - \cos \varphi)], \tag{57}$$

where the dimensionless constant  $r_2$  plays with respect to fluctuations a role analogous to that of  $r_1$  in Eq. (56). The angular dependence of the function  $X$  is illustrated in Fig. 2. Note the increasing alignment of the energy current at  $\varphi = 0$  for large values of  $k\lambda$ .

From Eq. (49), we find near the attenuation peak:

$$q_{eff}(\mathbf{k}) \simeq \frac{(1 + 2r_2)k^5 \lambda^2 \bar{h}^2}{4k\varphi_{inc}} \exp\left(-\frac{(k\lambda\varphi_{inc})^2}{2}\right), \tag{58}$$

$$(k\lambda)^{-1} \ll \varphi_{inc} \ll 1,$$

while for small  $k\lambda$  we have

$$q(\mathbf{k}) \simeq \frac{\pi(1 + r_2)k^5 \lambda^2 \bar{h}^2}{2}, \quad k\lambda \ll 1. \tag{59}$$

We compare the result in Eq. (59) with the prediction of viscous models such as the one by Keller<sup>35</sup>

$$q(\mathbf{k}) \sim \frac{k^{7/2}h\nu}{g^{1/2}}, \quad \text{Keller}, \tag{60}$$

and the close-packing (CP) model<sup>29</sup>

$$q(\mathbf{k}) \sim \frac{g^{1/2}k^{5/2}h^3}{\nu}, \quad \text{CP}, \tag{61}$$

where  $\nu$  is the effective viscosity of the ice layer. A reasonable assumption in Eq. (59) is that  $\bar{h}^2 \sim h^2$ . We then see that to reproduce the resulting quadratic scaling in  $h$  in Eq. (59), a linear scaling in  $h$  for the effective viscosity must be assumed. The relationship is in line with both De Carolis *et al.*<sup>14</sup> and Sutherland *et al.*,<sup>32</sup> who obtained constitutive laws for  $\nu = \nu(h)$  by dimensional analysis.

We note that the wave attenuation in Eqs. (58) and (59) depends on the horizontal size of the ice bodies only indirectly through the dependence of the roughness coefficient  $r_2$  on the ice concentration  $C = \pi R^2n$ . The absence of  $R$  in the equation for  $q_{eff}$  is a consequence of treating the ice layer as an almost featureless continuum.

This prompts us to look at diffusion as a result of the interaction of the incident wave with clumps of ice of size  $\lambda$ . The correlation length  $\lambda$  plays indeed a role analogous to that of the floe diameter in the case of large floes. A simple two-dimensional wave scattering model developed in Wadhams,<sup>51</sup> in the case of floes with diameters of the order of tens of meters, proved indeed that for larger floes the roll-over peak is critically dependent on the floe diameter.

The dependence on  $R$  of  $q_{eff}$  resurfaces if one considers the limit of uniformly distributed ice, in which case the only surviving fluctuations are those produced by Poisson statistics at the scale of the individual ice bodies. This corresponds to making the substitution  $\lambda \rightarrow R$  in Eq. (58). The magnitude of  $q_{eff}$  is further reduced if one disregards the mutual interaction of the ice bodies, which is appropriate only for  $C \ll 1$ . The flow perturbation can be shown in this case to be a quadrupole field, corresponding to the polarizability of an individual body  $\alpha_2 \sim k^2 R^4 h$ . From Eqs. (17), (34), and (45), the resulting wave would be

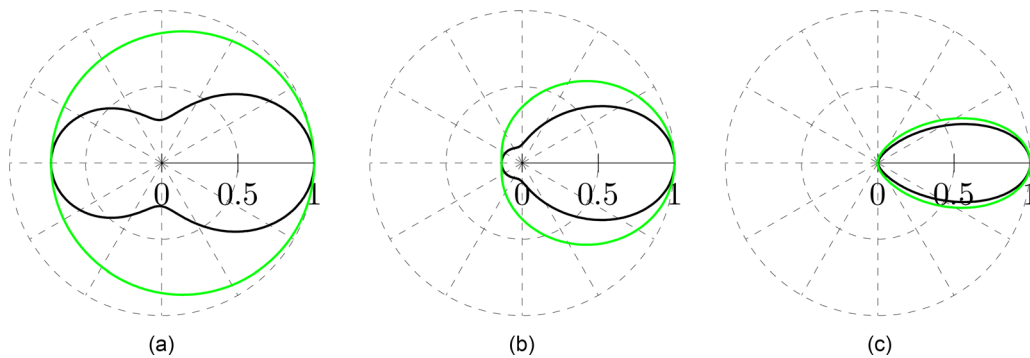


FIG. 2. Polar plot of the normalized energy current  $X(\mathbf{k}, \varphi)/X(\mathbf{k}, 0)$  for different values of  $k$  and  $r_2$ : (a)  $k\lambda = 0.4$ , (b)  $k\lambda = 1$ , (c)  $k\lambda = 2$ ; black line;  $r_2 = 0$  light line (green online).



$$q(\mathbf{k}) \sim \frac{\bar{n}}{k} (k^3 \alpha_2)^2 \sim C k^9 R^6 h^2, \quad C \ll 1, \quad (62)$$

which is going to be negligible in situations of oceanographic interest.

## VII. COMPARISON WITH OTHER MODELS

We can try to put some numbers in Eqs. (57) and (48) and compare the resulting predictions on  $q_{\text{eff}}$  with those by other wave attenuation models. We study the Keller's<sup>25</sup> and the CP model,<sup>29</sup> and the recent scattering-based model described in Meylan *et al.*<sup>52</sup> In the last case, a computer code is provided in the reference, which we have directly utilized in our analysis.

The results are illustrated in Fig. 3, considering ocean waves with wavelengths ranging from 15 to above 600 m, and several values of the parameters describing the ice layer. In this respect, we note the different meaning taken by the ice thickness  $h$  in the different approaches: for the model in Meylan *et al.*,<sup>52</sup>  $h$  is the actual thickness of the floes; in Keller<sup>25</sup> and in De Santi and Olla,<sup>29</sup> it is the effective thickness of

the ice layer, while the parameter  $\overline{h^2}$  fixes at most a fluctuation scale for  $h$  in Eqs. (57).

The general trends of variation for the parameters  $\lambda$  and  $\varphi_{\text{inc}}$  are illustrated in Fig. 3, panels (a) and (b). We note the clear rollover peaks in attenuation that are shifted to lower wavenumbers as the two parameters  $\lambda$  and  $\varphi_{\text{inc}}$  are increased.

In the scattering-based approach of Meylan *et al.*,<sup>52</sup> we have considered floes of radius  $R = 1$  m and  $h = 0.5$  m thickness, uniformly distributed at the water surface (hence  $\lambda = 0$ , with only discrete Poisson fluctuations present). In the case of Eq. (48), we have taken values  $\lambda = 25$  m,  $\varphi_{\text{inc}} = 10^\circ$ ,  $\overline{h^2} = 5 \times 10^{-4}$  m<sup>2</sup> for the correlation length of the fluctuation in the ice layer, the opening angle of the incident wave and the ice thickness variance, respectively, and we have set  $r_2 = 1$  in Eq. (57).

The attenuation rates predicted by the two scattering-based approaches are well-aligned only for waves longer than 200 m, for which the flexural rigidity of 1 m radius floes is expected to be

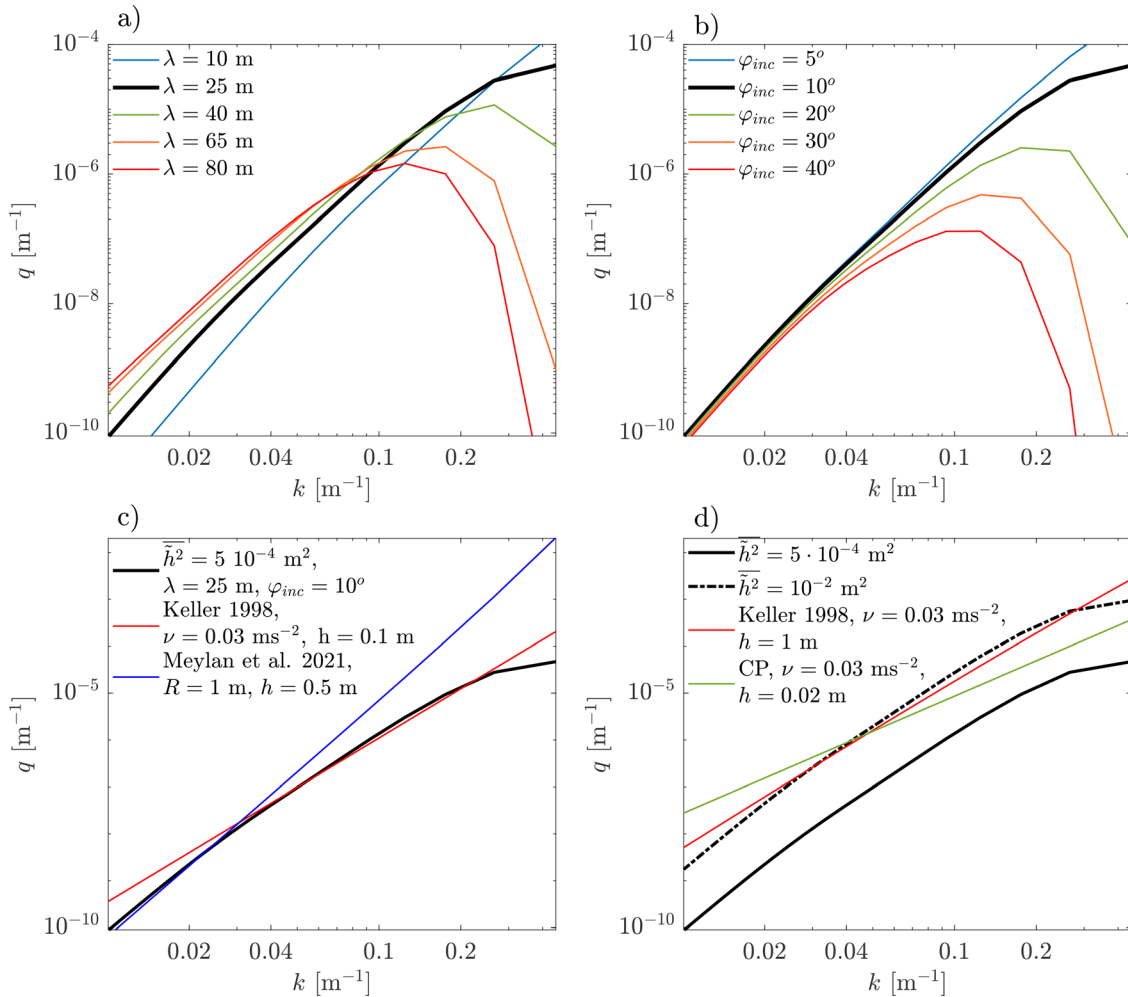


**FIG. 3.** Trends of variation for the wave attenuation  $q_{\text{eff}}$  as a function of  $\lambda$  and  $\varphi_{\text{inc}}$  [panels (a) and (b)] and comparison with other viscous and scattering-based models [panels (c) and (d)]. Black solid lines correspond to  $\overline{h^2} = 5 \times 10^{-4}$  m<sup>2</sup>,  $\lambda = 25$  m,  $\varphi_{\text{inc}} = 10^\circ$ , and  $r_2 = 1$  in all panels.

negligible. This behavior for very long waves is consistent with computational fluid dynamics simulations that consider the heterogeneous sea ice material composition and account for the wave–ice interaction dynamics.<sup>53</sup> Numerical results therein suggest that the mechanical sea ice response becomes independent of the detailed distribution of pancakes for wavenumbers smaller than  $0.016 \text{ m}^{-1}$ .

For wavelengths in the range  $30 - 200 \text{ m}$ , of interest for oceanographic applications, the effect of the ice cover inhomogeneity in Eq. (48) becomes significant. While scattering from uniformly distributed pancakes, as described within the approach in Meylan *et al.*,<sup>52</sup> produces attenuations almost proportional to  $k^5$  over the whole range of  $k$ , taking into account long-range fluctuations in the ice cover, as afforded by Eq. (48), reduces the exponent in the attenuation scaling to almost  $7/2$ . The scaling is comparable with the one predicted by the Keller’s model<sup>25</sup> [see Eq. (60)], in the case of an effective viscosity equal to that of grease ice,<sup>54</sup>  $\nu = 0.03 \text{ ms}^{-2}$  and thickness of the ice layer  $h = 0.1 \text{ m}$  [red curve in Fig. 3, panel (c)].

The result is non-trivial, suggesting that scattering by pancake-ice in the presence of long-range fluctuations in the ice-cover could lead to a wave damping comparable to the one due to pure viscous effects. We note the smallness of the thickness variance utilized,  $\overline{h^2} = 5 \times 10^{-4} \text{ m}^2$ , which could rise at most to  $\overline{h^2} = 1.5 \times 10^{-3} \text{ m}^2$  if the effect of roughness was neglected by setting  $r_2 = 0$  in Eq. (48). The smallness of  $\overline{h^2}$  is a further indication that the effect of fluctuations in the ice cover *a priori* should not be overlooked. The fact that the wave damping due to a fluctuation level of few centimeters is comparable with the one predicted by Keller’s model could at least partially explain the high values for the effective viscosity required by viscous models to reproduce experimental data.<sup>30,31</sup>

The effect on  $q_{\text{eff}}$  of varying  $\overline{h^2}$  is shown in Fig. 3, panel (d). A larger thickness variance in Eq. (48) has the same effect on attenuation as a larger effective thickness of the ice layer in Keller’s model. It is indeed possible to make the curves for the two models almost overlap [black dashed-dotted line and red continuous line in Fig. 3, panel (b)]. The same operation does not seem to be possible with the CP model.

### VIII. COMPARISON WITH EXPERIMENTS: ARCTIC SEA STATE PROGRAM DATA

We compare the predictions on wave attenuation derived in Secs. V–VII, with experimental data from wave-buoy deployed in ice fields in the Arctic.

The data considered in this section were collected in Autumn 2015 in the Beaufort Sea, as part of the Arctic Sea State program.<sup>4</sup> Wave data were supplemented by information on the properties of the ice cover (size, thickness, concentration, and composition of the ice bodies), which were supplied by the Arctic Shipborne Sea Ice Standardization Tool (ASSIST)<sup>55</sup> and sampling of the ice surface. Concurrently, the sea ice extension and its temporal evolution were monitored using satellite images acquired by synthetic aperture radar (SAR) systems.

SAR observations play a crucial role in the present analysis as they provide estimates of the correlation length of the ice field. Indeed, SAR images are generally two-dimensional maps of the Earth surface, which supply a description of the different targets in the scene with details imposed by the geometric resolution of the imaging sensor. The signal backscattered by the surface carries primary information

on both the roughness of the surface at the scale of the impinging electromagnetic radiation and the dielectric properties of the imaged target as well.<sup>56</sup> As sea ice and water have well distinct roughness and dielectric properties,<sup>57</sup> SAR sensors can provide a synoptic view of the field composition.<sup>22</sup>

Although for the MIZ a direct relation between the SAR signal and ice properties has not been established yet, there is evidence of a correlation between the ice thickness, surface roughness, and the radar cross section (i.e., the SAR signal).<sup>58</sup> Information on the correlation structure of the fluctuations in the ice cover can therefore be obtained through the analysis of the correlation function of the radar cross section. A robust technique to estimate the correlation function from SAR is based on evaluating the inverse fast Fourier transform (IFFT) of the power spectral density (PSD) computed from the two-dimensional radar cross section.<sup>59</sup> In order to remove the contribution of speckle noise at lag 0, a Butterworth filter is applied to the PSD before performing the IFFT.<sup>14,60</sup>

We focus on observations on the 1 November because of the availability of two SAR images acquired 2 h apart over the area where the array of wave buoys was in operation. The first acquisition is performed by the X-band (9.6 GHz) SAR system on-board satellite number 3 of the Cosmo-SkyMed (CSK) constellation at 15:46 UTC; the second one by the C-band (9.6 GHz) SAR operated by the Sentinel-1A (S1) belonging to the Copernicus mission at 17:20 UTC. The two SAR acquisitions are shown together with the location of the wave buoys in Fig. 4 and reveal a MIZ composed of grease, pancake, and small ice floes.

For the blue-highlighted regions shown in Fig. 4, the SAR spectral analysis is performed to determine the correlation functions along the

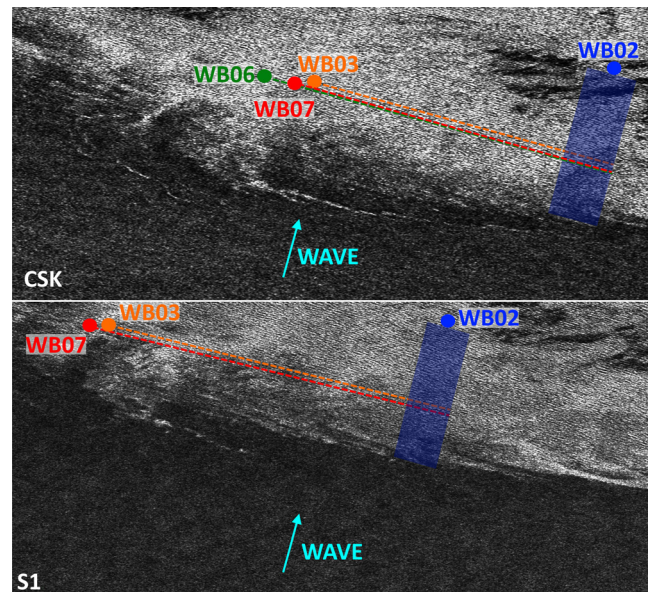


FIG. 4. Top panel: Cosmo-SkyMed image acquired at 15:46 UTC. Bottom panel: Sentinel-1A SAR image acquired at 17:20 UTC. Superimposed are the wave buoy locations at 15:30 UTC and 17:30 UTC, respectively. The cyan array indicates the incoming wave peak direction. Blue rectangles highlight the area in which sea ice properties are inferred. For both images, the spatial subset ( $-159.6^\circ \text{ E}$ ,  $-159.25^\circ \text{ E}$ )  $\times$  ( $72.60^\circ \text{ N}$ ,  $72.81^\circ \text{ N}$ ) is shown in the figure.

directions of the waves coming from the open ocean ( $\approx 224^\circ$  N).<sup>61</sup> As shown in Fig. 5, they are well fitted by Gaussian distributions of width  $\lambda = 26.83$  and  $\lambda = 19.52$  m for the CSK and S1 acquisitions, respectively. It is worth noting that although the incoming dominant waves induce a quasi-periodic modulation of the microwave signal about 110 m long, the inferred  $\lambda$  is well separated from this wavelength.

As shown in Fig. 4, buoy WB02 lies farthest inside the MIZ and is therefore taken as downstream reference buoy. However, none of the buoy pairs is aligned with the dominant wave direction (cyan arrow). The dotted lines identify the wavefronts at the location of the buoys; their distance to buoy WB02 defines the optical path along which wave attenuation is going to be evaluated. The sea ice properties in the transect between the wavefronts of the upstream buoys and buoy WB02 (blue region in Fig. 4), determine the measured wave attenuation.

Let us make the hypothesis that wave diffusion is the only attenuation mechanism for the incident waves. We can then use the value of  $\lambda$  from analysis of the SAR images to carry out a best-fit of the buoy data on wave attenuation with Eqs. (57) and (48), to retrieve the values of the remaining parameters  $\varphi_{inc}$  and  $\overline{h^2}$ ,

$$\min_{\overline{h^2}, \varphi_{inc}} \sum_i \left[ q_m(\mathbf{k}_i) - q_{eff}(\mathbf{k}_i; \overline{h^2}, \varphi_{inc}, \lambda) \right]^2, \quad (63)$$

where  $q_m$  are the measured data, obtained as described in Cheng *et al.*,<sup>30</sup> and reanalyzed to clear the data from any unwanted instrumental noise energy.<sup>34</sup> The procedure is detailed in the Appendix. We continue to assume  $r_2 = 1$  in Eq. (48). Best-fit samples of wave attenuation for measures close to the SAR acquisitions are reported in Fig. 6. Red circles represent the wave-buoy attenuation rates  $q_m$ . Black lines show attenuation rates computed with Eqs. (48) and (57). The top panels show the attenuation rates measured at 15:30 UTC and are thus related to the CSK acquisition, while the bottom panels show the attenuation rates measured at 17:00 UTC and 17:30 UTC and are related to the S1 acquisition.

In all cases, the fitting procedure can reproduce the structure of the rollover peak. We find in particular good agreement between the values of  $\varphi_{inc}$  estimated by the fitting procedure and

the ones from analysis of the angular spectrum from buoy data (see Fig. 7).

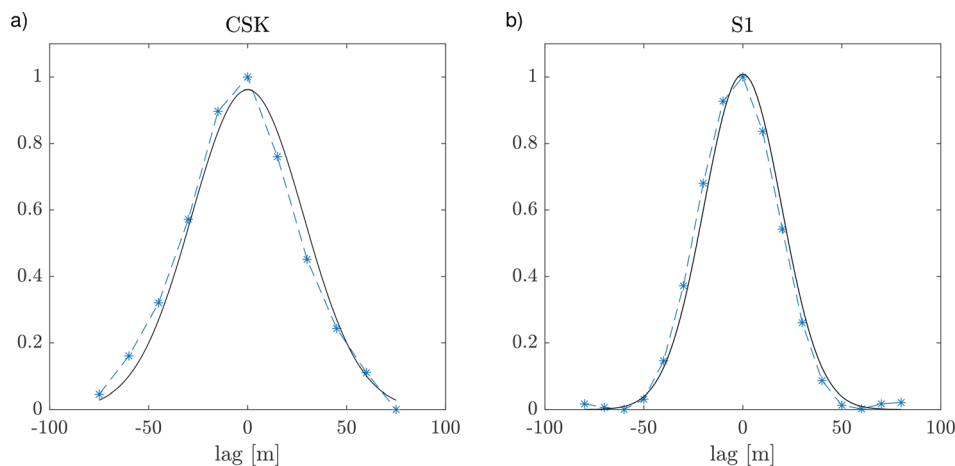
The inferred values for the variance,  $\overline{h^2} = 0.04\text{--}0.12$  m<sup>2</sup>, instead, are large compared to the expected values of the sea-ice thickness  $h \approx 0.1$  m at 16:54 UTC and  $h \approx 0.15$  m at 18:00 UTC, reported in the region of interest by the Arctic Shipborne Sea Ice Standardization Tool (ASSIST).<sup>55</sup> At the present stage, it is not clear whether the difficulty could be solved by a redefinition of  $h$  and  $r_2$ , or is a signal of actual smallness of the diffusion contribution to wave attenuation.

As shown in Fig. 7, the inferred  $\varphi_{inc}$  well separates the dominant wave from another wave packet coming further from the west. The amplitude of the second wave packet increases with time, while the energy and the opening angle of the dominant wave decrease with time. It is worth noting that the directional spectra measured at the same time by different upstream buoys show significant differences, despite the buoy locations being sufficiently tight (see Fig. 4). The temporal evolution of the directional spectra of WB02 (red curves in Fig. 4), in particular, is difficult to interpret, with the peak wave energy at 17:00 UTC higher than the one of the other time stamps and the one of the upstream buoys.

## IX. CONCLUSION

We have studied the diffusion of gravity waves generated in a pancake-ice covered inviscid water column, with special focus on the role of random spatial variations in the thickness and the concentration of the ice layer. We have modeled pancake-ice as a horizontally inextensible, but otherwise stress-free continuum. At the scale of the individual ice body, the dynamics is realized most simply by assuming that the bodies are in close contact without the possibility of rafting.

Two mechanisms in the generation of wave radiation can be identified: vertical motions of the bodies, which generate radial waves, and horizontal motions of the bodies, which generate a dipole field with lobes along the direction of propagation of the incident wave (both motions defined relative to the unperturbed wave field). The contribution from higher order multipoles appears to be negligible for bodies much smaller than a wavelength. The dipole radiation is itself negligible if instead of a layer composed of many ice bodies, we have a continuous ice slab with an immersed surface of vanishing roughness.



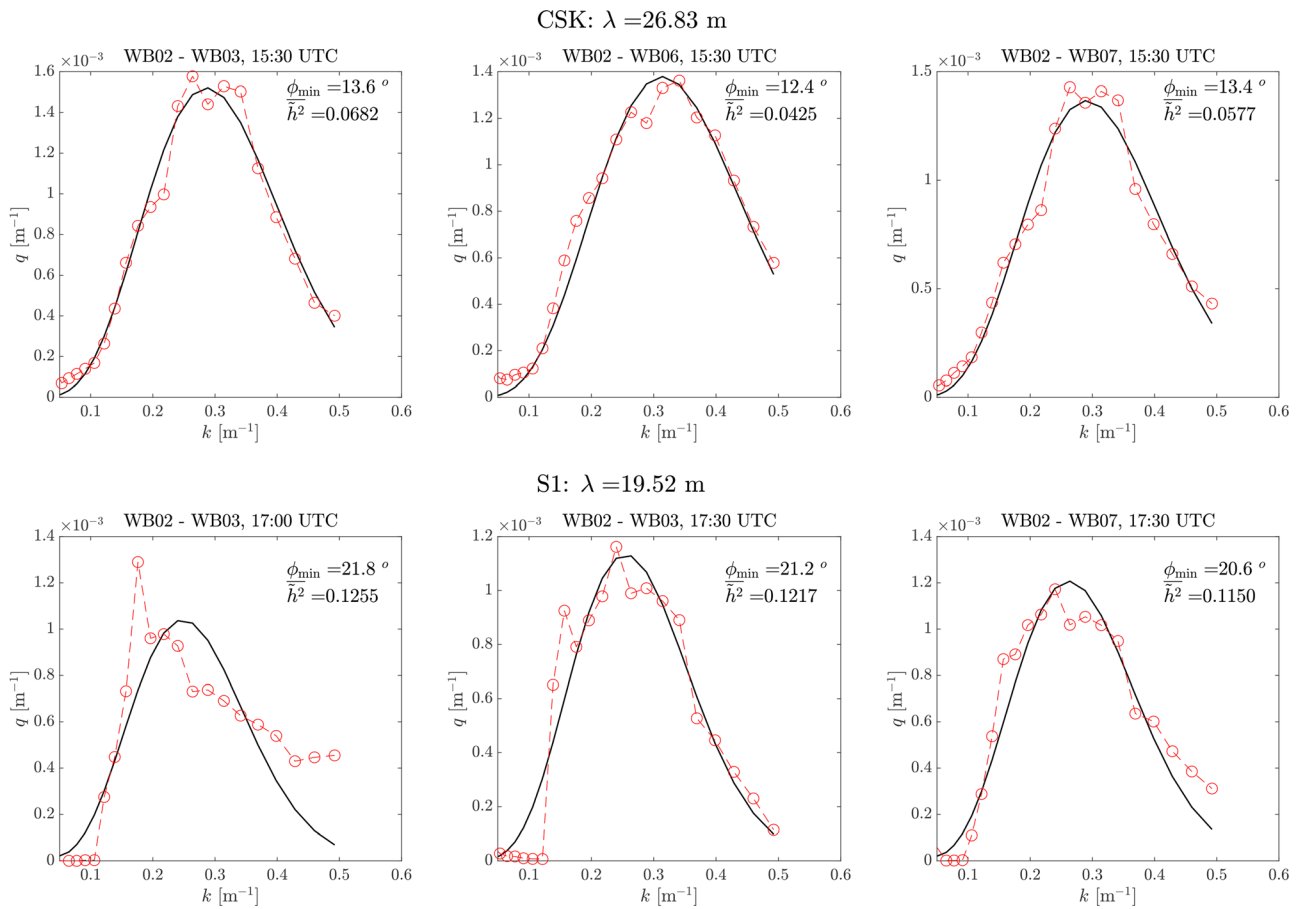


FIG. 6. Examples of wave buoys' attenuation data fitted by minimizing Eq. (63) for measurements concomitant with SAR acquisitions.

We have evaluated the contribution to wave attenuation from diffusion in terms of the fraction of the diffused energy that is radiated at angles exceeding the opening angle  $\phi_{inc}$  of the incident wave.

We have found that wave diffusion is stronger for waves with wavelength comparable to the correlation length  $\lambda$  of the fluctuations in the ice layer. The phenomenon is associated with a contribution to wave attenuation, which is itself maximum near  $\lambda$ , thus providing a mechanism for rollover similar to the one described in Wadhams,<sup>51</sup> where the role of the parameter  $\lambda$  was played by the radius of the individual floes. For  $\lambda$  close to the observed rollover peak, it is indeed possible, with reasonable values of the amplitude of the fluctuations in the ice thickness and concentration, to generate an attenuation of the incident waves comparable to what is observed in field experiments. One may expect that similar phenomena could play a role in wave energy harvesting by large assemblies of wave energy converters.<sup>62</sup> The contribution to diffusion from the discreteness of the ice bodies, instead, is negligible for bodies much smaller than a wavelength and is further reduced if the mutual interaction of the bodies is not taken into account.

We have compared the results of the theory with buoy data from the Sikuliaq campaign in Autumn 2015 in the Arctic,<sup>4</sup> and SAR images available in that region in the same period.<sup>14</sup> We have followed the

approach by Thomson *et al.*<sup>34</sup> to eliminate spurious instrumental noise contributions to the development of a rollover peak, and we have found that rollover persists in all analyzed data. We have found that the roughness map of the SAR images is characterized by spatial fluctuations peaked in the rollover region, which furnishes indirect evidence to possible inhomogeneity of the ice cover at that scale.

We have carried out a best-fit analysis of the attenuation data with the inferred value of  $\lambda$ , in the assumption that wave diffusion is the only mechanism at play. The resulting fluctuation levels of  $h$  are somewhat large, but not to the point of dismissing the possibility of an important role of diffusion in the attenuation process. A more definite statement would require going beyond the qualitative description of the layer structure afforded in Sec. VI.

Attenuation by diffusion could also explain the puzzling observation that fitting experimental data by viscous models requires an effective viscosity dependent on the ice thickness. As illustrated in Sec. VII, we see in fact that the small wavenumber scaling of the attenuation obtained by a diffusion-based model can be reproduced by viscous models such as the one by Keller and the CP model only by assuming an effective viscosity  $\nu$  linearly proportional to the ice thickness.<sup>14</sup>

The analysis in this paper is based on rough modeling assumptions on the dynamics of the ice layer, which are not too different from

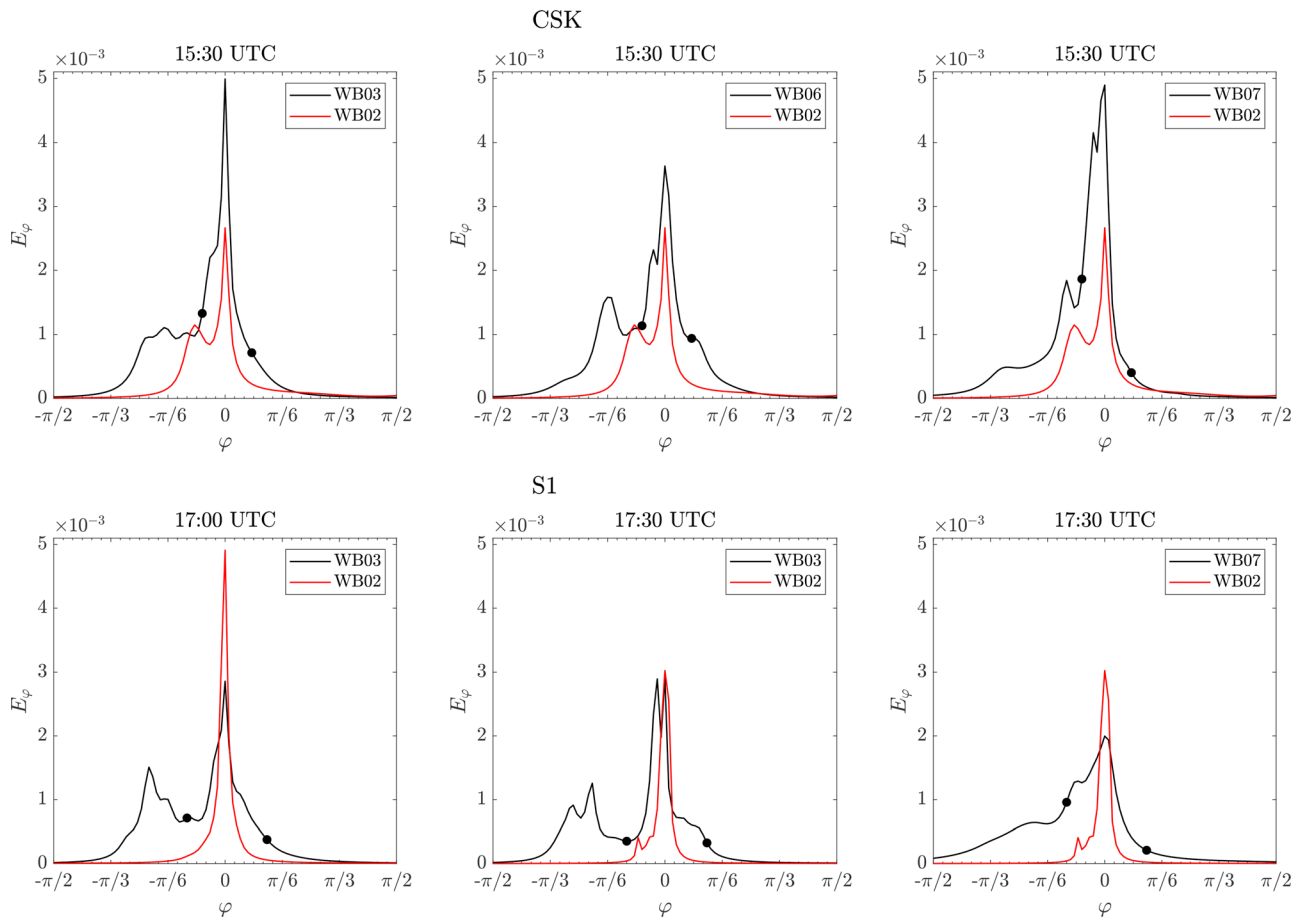


**FIG. 7.** Wave energy spectra of the upstream buoys (black curves) and the downstream buoy (red curves) integrated over wavenumber  $k$ . Circles indicate the values of  $\varphi_{mc}$  obtained by minimizing Eq. (63). The buoy pairs reported are the same as in Fig. 6.

those at the basis of the mass-loading model.<sup>41,42,51</sup> The average wave dynamics obtained in the present theory coincides in fact with what would be obtained using a mass-loading model. An obvious question is whether the inextensibility hypothesis adopted in the present paper would still hold if the ice bodies in the layer interacted hydrodynamically rather than by contact forces. A numerical study of the matter is under way, following the approach detailed by Kagimoto and Yue<sup>40</sup> and adopted more recently by Meylan *et al.*<sup>52</sup>

**ACKNOWLEDGMENTS**

This work has been supported by the Italian Piano Nazionale Ricerche in Antartide (Project WAMIZ, Grant No. PNRA18/\_00109) and by the EU FP7 Project ICE-ARC (Grant Agreement No. 603887). The present work is a contribution to the Year of Polar Prediction (YOPP), a flagship activity of the Polar Prediction Project (PPP), initiated by the World Weather Research Programme (WWRP) of the World Meteorological Organisation (WMO). We acknowledge the WMO WWRP for its role in coordinating this international research activity. The CSK product used in this work was delivered by ASI (Italian Space Agency)

under the ASI licence to use ID 714 in the framework of COSMO-SkyMed Open Call for Science. The Sentinel-1A used in this work was freely delivered by ESA through the Copernicus Open Access Hub (<https://scihub.copernicus.eu>).

**APPENDIX: DATA ANALYSIS PROCEDURE**

The spectral noise energy  $E_n(k)$  is assumed to follow the power-law  $k^{-2}$  in the spectral tail above the peak with equivalent noise height  $H_n = 0.1$  m. The attenuation rates,  $q_m$ , can be estimated from the measured attenuation,  $q_b$ , as follows:

$$q_m(k) = q_b(k) + \frac{1}{D} \left[ \frac{1 + E_n(k)/E_D(k)}{1 + E_n(k)/E_U(k)} \right], \tag{A1}$$

where  $E_U$  and  $E_D$  are the noise-free, omni-directional wave energy spectra of the upstream and the downstream buoy, respectively, and  $D$  is the distance traveled by the waves between the couple of buoys. Note that the energy bias negligibly affected the attenuation rates  $q_m$ , meaning that data processing performed by Ref. 30 already properly accounted for noise contamination.

22 March 2024 10:51:34

## DATA AVAILABILITY

The data that support the findings of this study are available from the corresponding author upon reasonable request.

## REFERENCES

- <sup>1</sup>V. Squire, "Of ocean waves and ice sheets," *Annu. Rev. Fluid Mech.* **27**, 115–168 (1995).
- <sup>2</sup>J. Thomson and W. E. Rogers, "Swell and sea in the emerging arctic ocean," *Geophys. Res. Lett.* **41**, 3136–3140, <https://doi.org/10.1002/2014GL059983> (2014).
- <sup>3</sup>C. L. Parkinson and J. C. Comiso, "On the 2012 record low arctic sea ice cover: Combined impact of preconditioning and an august storm," *Geophys. Res. Lett.* **40**, 1356–1361, <https://doi.org/10.1002/grl.50349> (2013).
- <sup>4</sup>J. Thomson, S. Ackley, F. Girard-Ardhuin, F. Ardhuin, A. Babanin, G. Boutin, J. Brozena, S. Cheng, C. Collins, M. Doble *et al.*, "Overview of the arctic sea state and boundary layer physics program," *J. Geophys. Res.: Oceans* **123**, 8674–8687, <https://doi.org/10.1002/2018JC013766> (2018).
- <sup>5</sup>V. A. Squire, "Of ocean waves and sea-ice revisited," *Cold Reg. Sci. Technol.* **49**, 110–133 (2007).
- <sup>6</sup>V. A. Squire, "Ocean wave interactions with sea ice: A reappraisal," *Annu. Rev. Fluid Mech.* **52**, 37–60 (2020).
- <sup>7</sup>P. Wadhams, F. Parmiggiani, G. De Carolis, and M. Tadross, "Mapping the thickness of pancake ice using ocean wave dispersion in SAR imagery," in *Oceanography of the Ross Sea Antarctica* (Springer, 1999), pp. 17–34.
- <sup>8</sup>G. D. Carolis, "Retrieval of the ocean wave spectrum in open and thin ice covered ocean waters from ERS synthetic aperture radar images," *Nuovo Cimento C* **24**, 53–66 (2001).
- <sup>9</sup>P. Wadhams, F. Parmiggiani, and G. De Carolis, "The use of SAR to measure ocean wave dispersion in frazil-pancake icefields," *J. Phys. Oceanogr.* **32**, 1721–1746 (2002).
- <sup>10</sup>G. D. Carolis, "SAR measurements of directional wave spectra in viscous sea ice," *Riv. Ital. Telerilevamento* **26**, 31–36 (2003).
- <sup>11</sup>P. Wadhams, F. Parmiggiani, G. De Carolis, D. Desiderio, and M. Doble, "SAR imaging of wave dispersion in antarctic pancake ice and its use in measuring ice thickness," *Geophys. Res. Lett.* **31**, L15305, <https://doi.org/10.1029/2004GL020340> (2004).
- <sup>12</sup>P. Sutherland and J.-C. Gascard, "Airborne remote sensing of ocean wave directional wavenumber spectra in the marginal ice zone," *Geophys. Res. Lett.* **43**, 5151–5159, <https://doi.org/10.1002/2016GL067713> (2016).
- <sup>13</sup>P. Wadhams, G. Aulicino, F. Parmiggiani, P. Persson, and B. Holt, "Pancake ice thickness mapping in the Beaufort sea from wave dispersion observed in SAR imagery," *J. Geophys. Res.: Oceans* **123**, 2213–2237, <https://doi.org/10.1002/2017JC013003> (2018).
- <sup>14</sup>G. De Carolis, P. Olla, and F. D. Santi, "SAR image wave spectra to retrieve the thickness of grease-pancake sea ice using viscous wave propagation models," *Sci. Rep.* **11**, 2733 (2021).
- <sup>15</sup>D. Masson and P. LeBlond, "Spectral evolution of wind-generated surface gravity waves in a dispersed ice field," *J. Fluid Mech.* **202**, 43–81 (1989).
- <sup>16</sup>L. G. Bennetts and V. A. Squire, "On the calculation of an attenuation coefficient for transects of ice-covered ocean," *Proc. R. Soc. A* **468**, 136–162 (2012).
- <sup>17</sup>M. H. Meylan and V. A. Squire, "Response of a circular ice floe to ocean waves," *J. Geophys. Res.: Oceans* **101**, 8869–8884, <https://doi.org/10.1029/95JC03706> (1996).
- <sup>18</sup>M. Meylan, L. Bennetts, C. Cavaliere, A. Alberello, and A. Toffoli, "Experimental and theoretical models of wave-induced flexure of a sea ice floe," *Phys. Fluids* **27**, 041704 (2015).
- <sup>19</sup>Z. Li, Y. Shi, and G. Wu, "Interaction of ocean wave with a harbor covered by an ice sheet," *Phys. Fluids* **33**, 057109 (2021).
- <sup>20</sup>A. L. Kohout and M. H. Meylan, "An elastic plate model for wave attenuation and ice floe breaking in the marginal ice zone," *J. Geophys. Res.: Oceans* **113**, C09016, <https://doi.org/10.1029/2007JC004434> (2008).
- <sup>21</sup>V. A. Squire and F. Montiel, "Evolution of directional wave spectra in the marginal ice zone: A new model tested with legacy data," *J. Phys. Oceanogr.* **46**, 3121–3137 (2016).
- <sup>22</sup>T. Toyota, C. Haas, and T. Tamura, "Size distribution and shape properties of relatively small sea-ice floes in the Antarctic marginal ice zone in late winter," *Deep Sea Res., Part II* **58**, 1182–1193 (2011).
- <sup>23</sup>M. J. Doble, M. D. Coon, and P. Wadhams, "Pancake ice formation in the Weddell sea," *J. Geophys. Res.: Oceans* **108**, 3209, <https://doi.org/10.1029/2002JC001373> (2003).
- <sup>24</sup>M. J. Doble, G. De Carolis, M. H. Meylan, J.-R. Bidlot, and P. Wadhams, "Relating wave attenuation to pancake ice thickness, using field measurements and model results," *Geophys. Res. Lett.* **42**, 4473–4481, <https://doi.org/10.1002/2015GL063628> (2015).
- <sup>25</sup>J. B. Keller, "Gravity waves on ice-covered water," *J. Geophys. Res.: Oceans* **103**, 7663–7669, <https://doi.org/10.1029/97JC02966> (1998).
- <sup>26</sup>R. Wang and H. H. Shen, "Gravity waves propagating into an ice-covered ocean: A viscoelastic model," *J. Geophys. Res.: Oceans* **115**, C06024, <https://doi.org/10.1029/JC05591> (2010).
- <sup>27</sup>H. Chen, R. P. Gilbert, and P. Guyenne, "Dispersion and attenuation in a porous viscoelastic model for gravity waves on an ice-covered ocean," *Eur. J. Mech., B: Fluids* **78**, 88–105 (2019).
- <sup>28</sup>G. De Carolis and D. Desiderio, "Dispersion and attenuation of gravity waves in ice: A two-layer viscous fluid model with experimental data validation," *Phys. Lett. A* **305**, 399–412 (2002).
- <sup>29</sup>F. D. Santi and P. Olla, "Effect of small floating disks on the propagation of gravity waves," *Fluid Dyn. Res.* **49**, 025512 (2017).
- <sup>30</sup>S. Cheng, W. E. Rogers, J. Thomson, M. Smith, M. J. Doble, P. Wadhams, A. L. Kohout, B. Lund, O. P. Persson, C. O. Collins *et al.*, "Calibrating a viscoelastic sea ice model for wave propagation in the arctic fall marginal ice zone," *J. Geophys. Res.: Oceans* **122**, 8770–8793, <https://doi.org/10.1002/2017JC013275> (2017).
- <sup>31</sup>F. D. Santi, G. De Carolis, P. Olla, M. Doble, S. Cheng, H. H. Shen, P. Wadhams, and J. Thomson, "On the ocean wave attenuation rate in grease-pancake ice, a comparison of viscous layer propagation models with field data," *J. Geophys. Res.: Oceans* **123**, 5933–5948, <https://doi.org/10.1029/2018JC013865> (2018).
- <sup>32</sup>G. Sutherland, J. Rabault, K. H. Christensen, and A. Jensen, "A two layer model for wave dissipation in sea ice," *Appl. Ocean Res.* **88**, 111–118 (2019).
- <sup>33</sup>J. Li, A. L. Kohout, M. J. Doble, P. Wadhams, C. Guan, and H. H. Shen, "Rollover of apparent wave attenuation in ice covered seas," *J. Geophys. Res.: Oceans* **122**, 8557–8566, <https://doi.org/10.1002/2017JC012978> (2017).
- <sup>34</sup>J. Thomson, L. Hošeková, M. H. Meylan, A. L. Kohout, and N. Kumar, "Spurious rollover of wave attenuation rates in sea ice caused by noise in field measurements," *J. Geophys. Res.: Oceans* **126**, e2020JC0166606 (2020).
- <sup>35</sup>V. Polnikov and I. Lavrenov, "Calculation of the nonlinear energy transfer through the wave spectrum at the sea surface covered with broken ice," *Oceanology* **47**, 334–343, <https://doi.org/10.1134/S0001437007030058> (2007).
- <sup>36</sup>A. K. Liu and E. Mollo-Christensen, "Wave propagation in a solid ice pack," *J. Phys. Oceanogr.* **18**, 1702–1712 (1988).
- <sup>37</sup>W. Perrie and Y. Hu, "Air-ice-ocean momentum exchange. Part 1: Energy transfer between waves and ice floes," *J. Phys. Oceanogr.* **26**, 1705–1720 (1996).
- <sup>38</sup>H. H. Shen and V. A. Squire, "Wave damping in compact pancake ice fields due to interactions between pancakes," in *Antarctic Sea Ice: Physical Processes, Interactions and Variability* (American Geophysical Union, 1998), **Vol. 74**, pp. 325–341.
- <sup>39</sup>D. Skene, L. Bennetts, M. Meylan, and A. Toffoli, "Modelling water wave overwash of a thin floating plate," *J. Fluid Mech.* **777**, R3 (2015).
- <sup>40</sup>H. Kagemoto and D. K. Yue, "Interactions among multiple three-dimensional bodies in water waves: An exact algebraic method," *J. Fluid Mech.* **166**, 189–209 (1986).
- <sup>41</sup>A. S. Peters, "The effect of a floating mat on water waves," *Commun. Pure Appl. Math.* **3**, 319–354 (1950).
- <sup>42</sup>J. B. Keller and M. Weitz, "Reflection and transmission coefficients for waves entering or leaving an icefield," *Commun. Pure Appl. Math.* **6**, 415–417 (1953).
- <sup>43</sup>M. A. Peter and M. H. Meylan, "The eigenfunction expansion of the infinite depth free surface green function in three dimensions," *Wave Motion* **40**, 1–11 (2004).
- <sup>44</sup>L. D. Landau and E. M. Lifshitz, *Fluid Mechanics* (Pergamon Press, 1987), Vol. 6.
- <sup>45</sup>J. D. Jackson, *Classical Electrodynamics* (Wiley, 1999).
- <sup>46</sup>M. Abramowitz, I. A. Stegun, and R. H. Romer, *Handbook of Mathematical Functions with Formulas, Graphs, and Mathematical Tables* (Dover, 1988).
- <sup>47</sup>L. D. Landau and E. M. Lifshitz, *Quantum Mechanics: Non-Relativistic Theory* (Elsevier, 2013), Vol. 3.

- <sup>48</sup>M. A. Peter and M. H. Meylan, "Infinite-depth interaction theory for arbitrary floating bodies applied to wave forcing of ice floes," *J. Fluid Mech.* **500**, 145–167 (2004).
- <sup>49</sup>M. Howe, "Wave propagation in random media," *J. Fluid Mech.* **45**, 769–783 (1971).
- <sup>50</sup>F. Montiel, V. Squire, and L. Bennetts, "Attenuation and directional spreading of ocean wave spectra in the marginal ice zone," *J. Fluid Mech.* **790**, 492–522 (2016).
- <sup>51</sup>P. Wadhams, "The seasonal ice zone," in *The Geophysics of Sea Ice* (Springer, 1986), pp. 825–991.
- <sup>52</sup>M. H. Meylan, C. Horvat, C. M. Bitz, and L. G. Bennetts, "A floe size dependent scattering model in two- and three-dimensions for wave attenuation by ice floes," *Ocean Modell.* **161**, 101779 (2021).
- <sup>53</sup>R. Marquart, A. Bogaers, S. Skatulla, A. Alberello, A. Toffoli, C. Schwarz, and M. Vichi, "A computational fluid dynamics model for the small-scale dynamics of wave, ice floe and interstitial grease ice interaction," *Fluids* **6**, 176 (2021).
- <sup>54</sup>K. Newyear and S. Martin, "Comparison of laboratory data with a viscous two-layer model of wave propagation in grease ice," *J. Geophys. Res.: Oceans* **104**, 7837–7840, <https://doi.org/10.1029/1999JC900002> (1999).
- <sup>55</sup>Climate and Cryosphere Arctic Sea Ice Working Group (CliC-ASIWG), "Arctic shipborne sea ice standardization tool" (15 March 2021).
- <sup>56</sup>G. Franceschetti and R. Lanari, *Synthetic Aperture Radar Processing* (CRC Press, 2018).
- <sup>57</sup>L.-L. Fu and B. Holt, *Seasat Views Oceans and Sea Ice with Synthetic-Aperture Radar* (Jet Propulsion Laboratory, California Institute of Technology, 1982), Vol. 81.
- <sup>58</sup>T. Toyota, S. Ono, K. Cho, and K. I. Ohshima, "Retrieval of sea-ice thickness distribution in the sea of okhotsk from alos/palsar backscatter data," *Ann. Glaciol.* **52**, 177–184 (2011).
- <sup>59</sup>J. S. Bendat and A. G. Piersol, *Random Data: Analysis and Measurement Procedures* (John Wiley & Sons, Hoboken, NJ, 2011), Vol. 729.
- <sup>60</sup>A. D. Goldfinger, "Estimation of spectra from speckled images," *IEEE Trans. Aerosp. Electron. Syst.* **18**, 675–681 (1982).
- <sup>61</sup>P. Stoica, R. L. Moses *et al.*, *Spectral Analysis of Signals* (Prentice Hall, NJ, 2005).
- <sup>62</sup>G. Tokić and D. K. Yue, "Hydrodynamics of large wave energy converter arrays with random configuration variations," *J. Fluid Mech.* **923**, R1 (2021).